Investigation of the Three-Dimensional Shock-Wave/Turbulent-Boundary-Layer Interaction Initiated by a Single-Fin

Jian Fang[1, 2], Yufeng Yao[3], Alexandr A. Zheltovodov[4], Lipeng Lu[1*]
[1]*National Key Laboratory of Science and Technology on Aero-Engine Aero-Thermodynamics, School of Energy and Power Engineering, Beihang University, Beijing 100191, China*

[2]*Department of Computer Science and Engineering, Science and Technology Facilities Council (STFC), Daresbury Laboratory, Warrington WA4 4AD, United Kingdom*

[3]*Faculty of Environment and Technology, Department of Engineering Design and Mathematics, University of the West of England, Bristol BS16 1QY, United Kingdom*

[4]*Khristianovich Institute of Theoretical and Applied Mechanics, Siberian Branch of Russian Academy of Science, Novosibirsk 630090, Russia*

* Corresponding author. Tel.: +86 1082317413. Email: lulp@buaa.edu.cn

E-mail: fangjian@buaa.edu.cn (J. Fang), yufeng.yao@uwe.ac.uk (Y. Yao), zhelt@itam.nsc.ru (A.A., Zheltovodov), lulp@buaa.edu.cn (L. Lu).

Three-dimensional (3D) shock-wave/turbulent boundary layer interaction (SWTBLI) of a hypersonic flow passing a single-fin mounted on a flat plate at Mach number 5 and unit Reynolds number 3.7×10^7 was conducted by a large-eddy simulation (LES) approach. The performed LES has demonstrated good agreements with experimental data in terms of mean flow field structures, surface pressure distributions as well as surface flow pattern. Furthermore, the shock-wave system, flow separation structure, and turbulence characteristics were all investigated by analyzing the obtained LES dataset. It was found that for this kind of 3D SWTBLI problem, the flow characteristics in different regions have been dominated by respective wall turbulence, free shear-layer turbulence, and corner vortex motions, in different regions. In the reverse flow region, near-wall quasi-streamwise streaky structures were observed just beneath the main separation vortex, indicating that the transition of the pathway of the separation flow to turbulence may occur within a short distance from the reattachment location. The obtained LES results have provided a clear and direct evidence of the primary reverse flow and the secondary separation flow being essentially turbulent.

Nomenclature

C_f = skin friction coefficient

K = turbulent kinetic energy

M = free stream Mach number

M_n = conical-cross Mach number

p = static pressure

P_W = mean wall pressure

R, β, φ = virtual conical origin coordinates

Re = unit Reynolds number

t = time

T = static temperature

T^* = total temperature

u,v,w = velocity components in the Cartesian x,y,z directions

u_{vd} = Van Driest transformed mean streamwise velocity

u_β, u_φ = velocity components along the β and the φ directions in the VCO coordinates system

u_τ = wall friction velocity

x,y,z = Cartesian coordinates

β_1 = deflection angle of the fin

Δt = time step

δ, δ^*, θ = the 99% thickness, displacement thickness and momentum thickness of the boundary layer

ρ = density

λ_{ci} = swirling strength

Ω = vorticity magnitude

$\bar{\ }$ = (time) averaged quantity

$\langle\ \rangle$ = Favre averaged quantity

Subscripts

n = normal direction

R = R direction component

s = streamwise component

W = value at the wall

0 = reference value

Superscripts

′ = fluctuation from time averaged mean value

″ = fluctuation from Favre averaged mean value

+ = non-dimensionalization by the inner scales of boundary layer

I. Introduction

AS one of the most important flow features in high-speed flight, the phenomenon of shock-wave/turbulent boundary layer interaction (SWTBLI) has been studied persistently for more than sixty years. Despite that, some fundamental flow mechanisms are still not completely understood yet and the prediction of its aerodynamic performance is also unsatisfactory. [1] Compared with some two-dimensional (2D) and quasi-three-dimensional (q3D) SWTBLIs (i.e. those flows exhibiting homogeneity along the transverse direction, such as, a compression corner and/or an impinging oblique shock-wave/boundary layer interaction), the inhomogeneous fully three-dimensional (3D) SWTBLI problem is much less studied and understood [2], although it occurs in real flow problems and has significant effects on the performances of supersonic aircraft inlets and control surfaces. Therefore, further research of 3D SWTBLI problems is of great importance in understanding their underlying flow physics and mechanisms, as well as improving the aerodynamic performance of systems in which these flows are present.

Among various 3D SWTBLI test configurations, a supersonic/hypersonic flow passing a sharp single-fin mounted on a flat plate has been proposed and extensively studied due to its simple geometry and critical flow features observed. [2-4] In this flow configuration, a swept shock-wave is generated from the leading edge of a sharp semi-infinite single-fin and it interacts with a turbulent boundary layer developed along the flat plate. The shock-wave is smeared when it penetrates into the viscous boundary layer and disturbs flow upstream and downstream of the inviscid shock-wave. This was observed in the early research by Token [5] who reported that the flow structures of the 3D single-fin were dominated by a large longitudinal vortical structure which aligns on the flat plate and its vortex core has shown a remarkable conical shape with a flattened elliptical cross-section. This quasi-conical flow

characteristic was later confirmed by many other investigators. [6-14] Consequently, a spherical polar coordinate system has been widely used as a proper framework for the analysis of this kind of flows. With the varying of the shock-wave strength (via incoming flow Mach number and fin deflection angle), the flow topology can change significantly. Zheltovodov [9,15] and Zheltovodov et al. [7,16] identified a total of six regimes as seen from a 3D single-fin flow field, according to the surface flow patterns observed by oil-flow visualization on the plate surface. These regimes characterize the development of the primary convergence lines S1 and divergence lines R1 respectively associated with a boundary layer separation and reattachment, as well as the secondary convergence and divergence lines S2 and R2 which correspond to the secondary flow separation and reattachment in the 3D SWTBLI region. Along with an incipience and monotonic growth of a primary separation zone between the lines S1 and R1 in Regimes II-VI, and with a gradual increase of the shock-wave strength, a secondary flow separation behavior inside this zone is a critical flow phenomenon. Remarkably, it was found from experimental observations [15-17] that the secondary separation appears initially in Regime III, then begins to fade in Regime IV and disappears in Regime V, then finally reappears in Regime VI.

The mechanism of the observed appearance, disappearance and reappearance of the secondary separation at monotonically increasing fin deflection angle is still unclear, despite some experimental researchers having proposed the possible connection between this phenomenon and the state of the reverse flow (i.e. laminar or turbulent) in terms of the conditions of either conically subsonic or supersonic near-wall cross flow extending from the divergence line R1 to the convergence line S1.[3,12,15] Zheltovodov and Schülein [7] and Zheltovodov et al. [16] applied a sand-grain roughness strip placed along the primary attachment line R1 to trigger the laminar-turbulent transition of the reverse cross-flow in the vicinity of the fin. Such forced turbulization of the reverse flow could suppress probably a laminar secondary separation in Regimes III and IV but not a turbulent separation realized in Regime VI. The secondary separation in Regime VI reappears when the embedded normal shock-wave in the reverse flow reaches a critical strength to force the turbulent separation in a conically-supersonic cross flow. [7,15,16] Some comprehensive reviews on the flow physics in a 3D SWTBLIs have been done by Knight et al.,[3] Panaras,[4] Zheltovodov and Schülein,[7] Settles and Dolling,[18] Bogdonoff, [19] and more recently summarized by Zheltovodov and Knight. [20]

The above hypotheses need to be further verified and confirmed by detailed analysis of the development of the turbulent flow under such experimental conditions. However, due to the nature of strong non-equilibrium flow in 3D

SWTBLI, especially when the state of the reverse flow could possibly change during the process, numerical simulation based on Reynolds-averaged Navier–Stokes (RANS) equations with standard turbulence models is not very reliable for this kind of flow. [3,21-23] Panaras [24,25] has pointed out the inadequacy of the Boussinesq's equation in predicting strong cross-flow separation generated in the fin/plate configuration. Reviews of numerical predictions of 3D SWTBLIs with existing turbulence models were recently carried out by Knight et al. [3], Zheltovodov and Knight [20], and Panaras. [26]

Given the difficulty of extracting detailed turbulence information from both RANS predictions and wind tunnel measurements, large-eddy simulation (LES) may be a better choice for studying this kind of 3D SWTBLI, as it can provide detailed flow information to further understand the underlying turbulence mechanisms. However, most LES and direct numerical simulation (DNS) research in SWTBLI [27-30] are currently restricted to either 2D or q3D configurations due to the limitation of computational resources. With recent advances in high performance computing (HPC) technology, it is feasible to pursue an LES investigation of a full 3D SWTBLI configuration to further study the turbulence mechanisms e.g. Wang et al. [31] has recently conducted a LES study of SWTBLI wherein they considered the side-wall effect in a rectangular duct on the 3D corner separation and flow structures.

In the present study, LES of the 3D SWTBLI generated by a hypersonic Mach 5 flow passing over a sharp single-fin with a flow incidence of 23 degrees at a Reynolds number of 3.7×10^7/m is conducted. The flow condition is taken from the experiment of Schülein [32]. The results are validated against available experimental data, together with data analysis to realize both mean and instantaneous flow properties as well as turbulence mechanisms associated with the present 3D SWTBLI problem. The analysis of turbulent structures proves that the reverse flow beneath the main separation flow is fully turbulent and the secondary separation flow is essentially a turbulent separation at the studied flow condition.

II. Computational Details

A. Governing Equations and Numerical Method

Numerical simulation considers a compressible 3D unsteady flow governed by the spatial Favre-filtered Navier-Stokes (N-S) equations in a generalized curvilinear system. The classic dynamics subgrid scale (SGS) model [33,34] is used to determine the SGS eddy-viscosity model coefficients. The SGS heat flux is evaluated via an SGS Prandtl number, which is also calculated by the dynamic procedure during the time marching. The filtered N-S equations are

solved in a framework of a finite difference method, in which the convection terms are discretized and solved by using a recently developed seventh-order low-dissipative monotonicity-preserving (MP7-LD) scheme [35], which can effectively resolve small-scale turbulence motions away from shock-waves, similar to widely used high-order central schemes, and in the meantime preserve monotonicity near shock-waves. The scheme has been recently applied in the studies of various shock-wave/turbulence interaction problems [35-37]. The diffusion terms are solved by using the sixth-order compact central scheme [38]. After all the spatial terms are solved, the third-order TVD Runge–Kutta method [39] is used for the time integration.

B. Computational Domain and Mesh

The 3D SWTBLI of a single-fin studied herein is set to be at the same flow condition as that of the experiment of Schülein [32], in which the incoming flow Mach number is 5 and the fin deflection angle is $\beta_1 = 23°$. The flow configuration and its computational domain are sketched in Figure 1. The computational domain in the present study only contains the compression side of the fin, where the 3D SWTBLI happens, and the other side of the fin is discarded to simplify the simulation, consistent with other numerical simulations found in literature [40-42]. The reference length of the simulation is 1 mm and other reference parameters, such as density, temperature and velocity are taken from the incoming free-stream flow. The origin of the Cartesian coordinates is set at the leading edge of the fin on the plate. The inlet plane is positioned at $x = -20$ mm and is normal to the incoming flow direction. The outlet plane is at $x = 206$ mm, the spanwise domain starts from [0, 215 mm] at the inlet plane and extends to [78.3 mm, 215 mm] at the outflow plane. The wall normal size of the domain is $y = 50$ mm. Due to the employment of a sponge layer in all three directions, the size of the effective domain, which is marked with the thick lines in Figure 1 (b), is $[-20\text{mm}, 184.5\text{mm}] \times [0, 35\text{mm}] \times [0, 215\text{mm}]$, respectively. Considering the experimentally measured boundary layer thickness of the incoming boundary layer δ_0 is about 3.8 mm, the domain has a size of $[-5.3\delta_0, 18.6\delta_0] \times [0, 9.2\delta_0] \times [0, 56.6\delta_0]$.

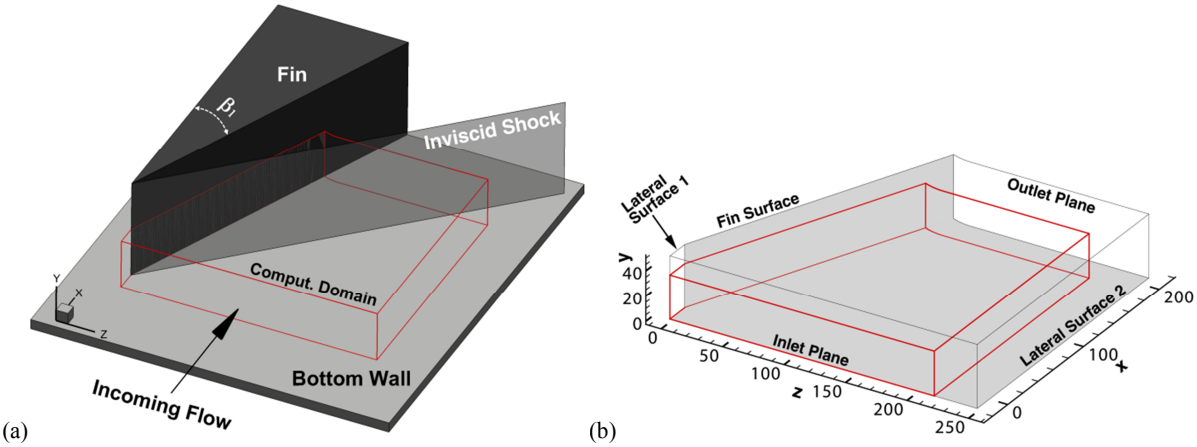

Figure 1. Sketches of: (a) the flow configuration and (b) the computational domain. The red thick lines represent the edges of the effective computational domain covered by the sponge layer.

The mesh was generated based on the criterion proposed by Sagaut [43] for LES of boundary layer flows, known as $\Delta x^+ = 50 - 100, \Delta y_1^+ = 1, \Delta z^+ = 10 - 20$. It should be noted that this criterion mainly applies to equilibrium boundary layer flows, which could be inadequate for non-equilibrium flow areas, such as separation and reattachment regions. The generated mesh has 240 grid points in the wall-normal direction (the η direction in computational domain), 1060 points in the streamwise direction (the ξ direction in computational domain), and 1420 points in spanwise direction (the ζ direction in computational domain), respectively. In the wall-normal direction, the mesh is firstly hyperbolically stretched in the near-wall region to make sure the distance of the first mesh points to the wall Δy^+ is below 1, then, the mesh spacing is uniformly distributed with the grid resolution of $\Delta y^+ \approx 15$. Here the viscous sub-layer scale is calculated based on the wall parameters of the incoming boundary layer. Similarly, the mesh is also hyperbolically stretched in the spanwise direction to make sure the grid resolution $\Delta z^+$is less than 1 at the first point near the fin sidewall surface and below 15 in the rest of the domain. The mesh spacing in the streamwise direction is uniformly distributed with a resolution of $\Delta x^+ \approx 20$ between the inlet and the fin leading edge location, and adjusted gradually after the leading edge, as shown in

Figure 2. In the region near the fin leading edge, the direction of the mesh in the spanwise direction is gradually turned into the fin normal direction to preserve smoothness and orthogonality, as shown in

Figure 2. The elliptic equations method [44] (namely TTM) is used to further smooth the mesh in the *x*-*z* plane. The total number of mesh points is over 360 million but the resolution might be still inadequate in the regions where complex and non-equilibrium flows exist. Because there are no general criteria for mesh for LES of non-equilibrium

flow, it is better to run a set of cases to conduct mesh independence study. However, the present studied case is too large to do so due to the limitation of the computing resource.

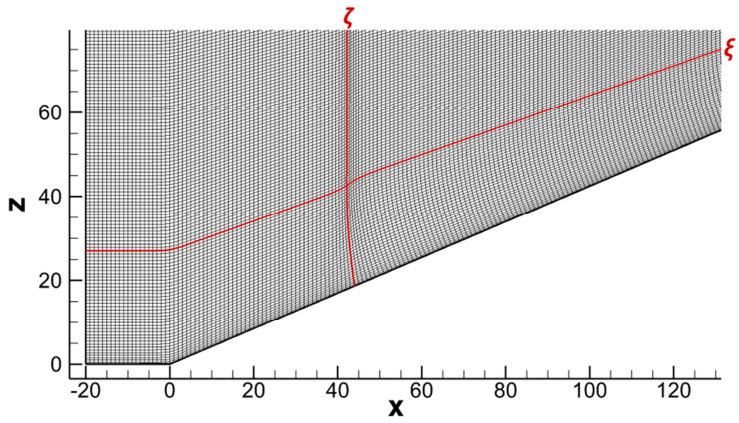

Figure 2 Distributions of the mesh around the leading edge on an *x*-*z* plane. The red lines mark two mesh lines along ξ and ζ directions. The mesh is drawn every 8 points in both directions.

C. Boundary Conditions

At the wall surfaces, as shown in Figure 1 (b), an isothermal no-slip condition with a fixed wall temperature $T_W = 4.39T_0$ (static temperature of the free-stream flow $T_0 = 68.3K$ in accordance with the experiment [32]). The boundaries of the outlet plane, the upper surface and the lateral surface 2 as shown in Figure 1(b) are treated with the non-reflective boundary condition [45,46]. To reduce the influence of numerical errors propagating to the boundaries, these boundaries are placed far away from the effective region by using the sponge layers with stretched coarse meshes and the low-order spatial filter [47]. At the lateral surface 1, instead of using the conventional periodical boundary condition in most q3D simulations, the free-slip boundary condition is applied. Therefore, the spanwise velocity component $w = 0$ is enforced and the derivatives of other primitive variables are also set to be zero at this boundary. According to the results of a precursor q3D turbulent boundary layer test [48], the influence of this treatment method is small and both the turbulent flow statistics and the main turbulence structures can be well preserved.

At the inlet plane, where the flow should be a fully developed turbulent boundary layer, either the widely used rescale and reintroduce method [49,50] or the synthetic turbulence method [30,51] would require a transitional flow region of at least 15 boundary layer thickness [52], leading to a great increase of mesh elements due to a large number of spanwise mesh points used in the present study. Alternatively, a time sequence of a fully developed turbulent flow at the same flow condition was generated by running another independent LES of a flat plate turbulent

boundary layer with a small domain size along the homogeneous spanwise direction, but still large enough to accommodate the near-wall turbulent streaks and the outer-layer wave numbers. The generated flow slices were then introduced to the main LES via the inlet plane by replicating itself along the spanwise direction and using the hybrid supersonic/subsonic inflow condition [53]. A similar inflow turbulence generation method was adopted by Gao et al. [54] for an LES of turbulence with a full 3D geometry and good agreement of the LES with measured data was shown. The present LES predictions of inflow boundary layer parameters and the comparison with the experiment of Schülein [32] at the location of 20 mm upstream of the leading edge of the fin are given in Table 1 and good agreement is shown in terms of boundary layer parameters.

Table 1 Incoming Boundary Layer Parameter

Line	M	Re	δ, mm	δ^*, mm	θ, mm	T^*, K	T_0, K	T_W, K
Experiments[32]	5.0	37×10^6/m	3.8	1.6	0.16	410	-	300 ± 5
Present LES	5.0	37×10^6/m	3.85	1.60	0.17	410	68.3	300

III. Results and Discussions

The LES time step is $\Delta t = 1.81 \times 10^{-8}\ s$, which is equivalent to $\Delta t^+ = 9.8 \times 10^{-2}$ in the wall viscous scale. The simulation persists for a total time of $t = 0.002$ s, and for every 300 time steps an instantaneous flow sample is saved, resulting in a total of 486 samples collected for data analysis after the simulation is statistically stationary. It should be noted that the current LES time is only about half of the testing time of $\tau = 20\, L/U_\infty$ recommended by Hornung [55], due to the limitation of HPC resource for a longer time integration.

A. Validation

The distribution of the Van Driest transformed mean streamwise velocity u_{vd}, at x = -2 mm is reported in Figure 3. u_{vd} is defined as,

$$u_{vd} = \int_0^{\langle u \rangle} \bar{\rho}/\bar{\rho}_W \, d\langle u \rangle, \tag{1}$$

From Figure 3, a good agreement between the present LES results and the classic law of the wall in both the linear sub-layer and the log-layer regions can be confirmed.

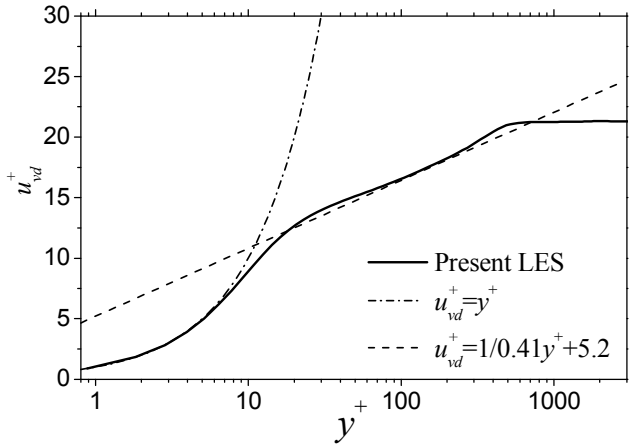

Figure 3 Distributions of Van Driest transformed mean streamwise velocity at x = -2 mm

Consistent with Morkovin's hypothesis, the density-scaled turbulence intensity $u_{i,RMS}$, which is defined as,

$$u_{i,RMS} = \sqrt{\frac{\bar{\rho}}{\bar{\rho}_W}\langle u_i'' u_i'' \rangle} \tag{2}$$

is reported in Figure 4 in terms of the inner-layer and the outer-layer coordinates. In Eq. (2), u_i is the velocity component. According to Figure 4, the results of the present LES in the undisturbed boundary layer region are in good agreement with that of incompressible DNS data (e.g. Spalart[56] and Wu & Moin[57]), compressible DNS at Mach=1.3 (Pirozzoli et al. [58]), as well as low-speed boundary-layer experiments (e.g. Purtell et al. [59] and Erm & Joubert[60]), in both the near-wall region and the outer-layer of the boundary layer, which indicates that Morkovin's hypothesis is still applicable for the high-speed flow at M = 5.

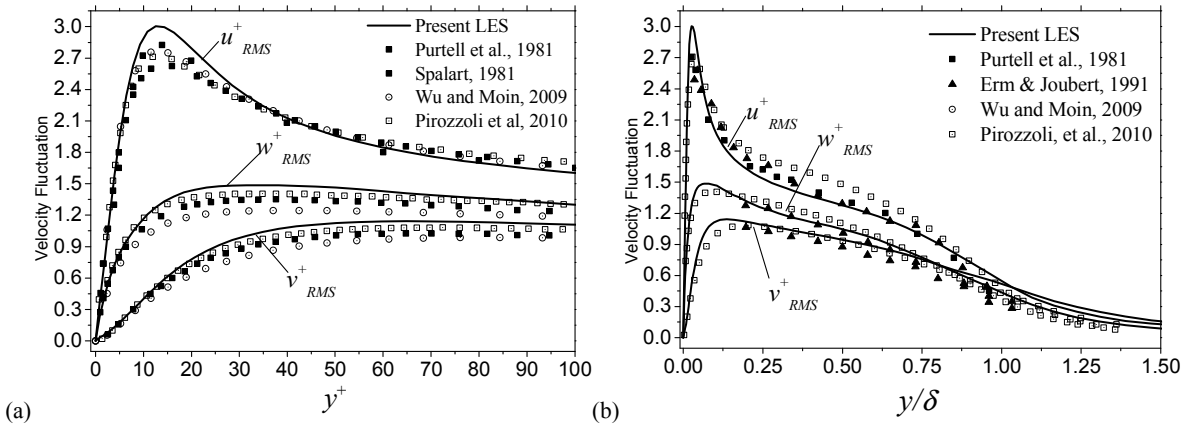

Figure 4 Density-scaled turbulence fluctuations in: (a) inner scaling and (b) outer scaling at x = -2 mm

It is thus concluded that the flow statistics in the undisturbed boundary layer upstream of the leading edge of the fin are in good agreement with the boundary layer theory, experimental measurements and other DNS data, which validates the accuracy of the present LES in the equilibrium flow region.

As described in the introduction, one of the main features of the 3D fin flow is the appearance of both primary and secondary flow separation. According to the flow regime map of Zheltovodov [15], and Zheltovodov et al. [16,20], both the primary and the secondary separations should appear at the present flow condition. The 3D flow separation and attachment patterns are characterized by the convergence and the divergence of the skin-friction-lines respectively as sketched in Figure 5 (a). The comparisons of the angle of the separation line S1, the reattachment line R1 and the secondary separation line S2 between the experimental measurements of Schülein and Zheltovodov [10] and present LES are shown in Figure 5 (b). The agreement between the present LES and experiments is found to be satisfactory.

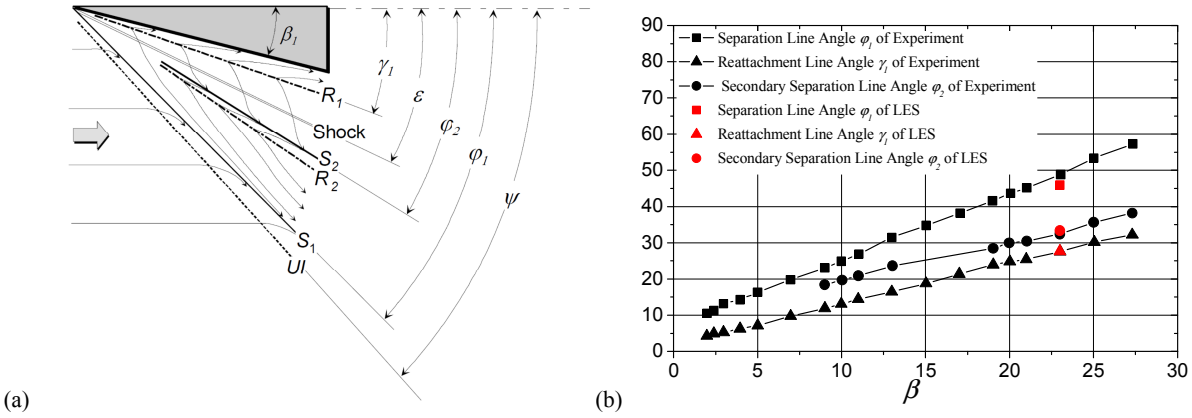

(a) (b)

Figure 5 The definition of the angles of the separation and reattachment lines (a) and their distributions in the experiment and the present LES (b)

The wall pressure distributions at the five cross sections of x = 83mm, 93mm, 123mm, 153mm, 183mm are compared with the measurements of Schülein[32] in Figure 6 (a), which shows good agreement between the LES predictions and the experimental measurements. The reattachment (or divergence) lines can also be reflected by the local peaks of the wall pressure distribution.

The distributions of mean skin friction coefficients C_f along x=83 mm, 123 mm, 163 mm, and 183 mm are shown in Figure 6 (b), and also compared with the experimental data of Schülein[32]. C_f at the bottom wall is defined as,

$$C_f = \frac{\mu_W \sqrt{\left(\frac{\partial \langle u \rangle}{\partial y}\Big|_{y=0}\right)^2 + \left(\frac{\partial \langle w \rangle}{\partial y}\Big|_{y=0}\right)^2}}{\frac{1}{2}\rho_0 u_0^2} \tag{2}$$

The agreement of the skin friction coefficient between LES and the measurement is overall acceptable in the region away from the fin's sidewall, except for the corner region, where the rapid increase of C_f and its high peak value measured in the experiment are somehow largely under-predicted in the present LES. The under-prediction of C_f is possibly attributed to the inadequacy of the mesh resolution near the reattachment line, where flow is in a strong non-equilibrium state and the mesh criterion of Sagaut does not apply. The under-prediction C_f in the corner region was also reported in RANS simulations at the same conditions by using the Reynolds stress model (RSM) [61] and standard Spalart-Allmaras (SA) model [62] respectively. The RSM model was found to improve C_f predictions against the SA model. Therefore, the under-prediction of C_f in this 3D configuration needs to be carefully investigated by conducting joint experimental/computational fluid dynamics research in the future.

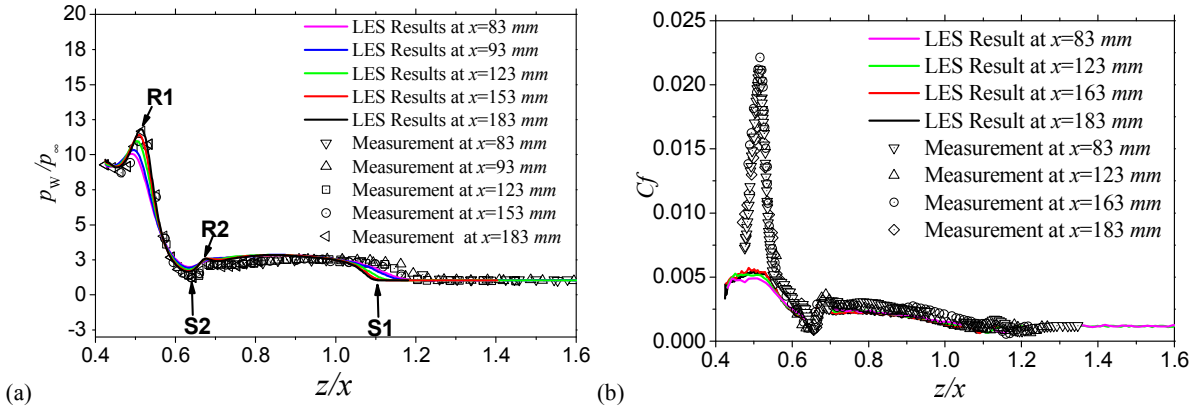

Figure 6 The distributions of wall pressure (a) and skin friction coefficient (b) at several *x*-locations.

B. Shock-Wave Structures

As introduced above, the nature of the flow field of the 3D single-fin is of quasi-conical type, except for an initial region in the vicinity of the fin's leading edge. Beyond this initial region, flow topological features appear to emanate from a single point, named the "Virtual Conical Origin" (VCO) and a Spherical coordinate system (R, β, φ) is an appropriate coordinate frame to study these flows[63]. In the present study, VCO is located at (-22.57mm, 0mm, -14.91mm), determined by the intersection of S1, R1 and S2, as sketched in Figure 7.

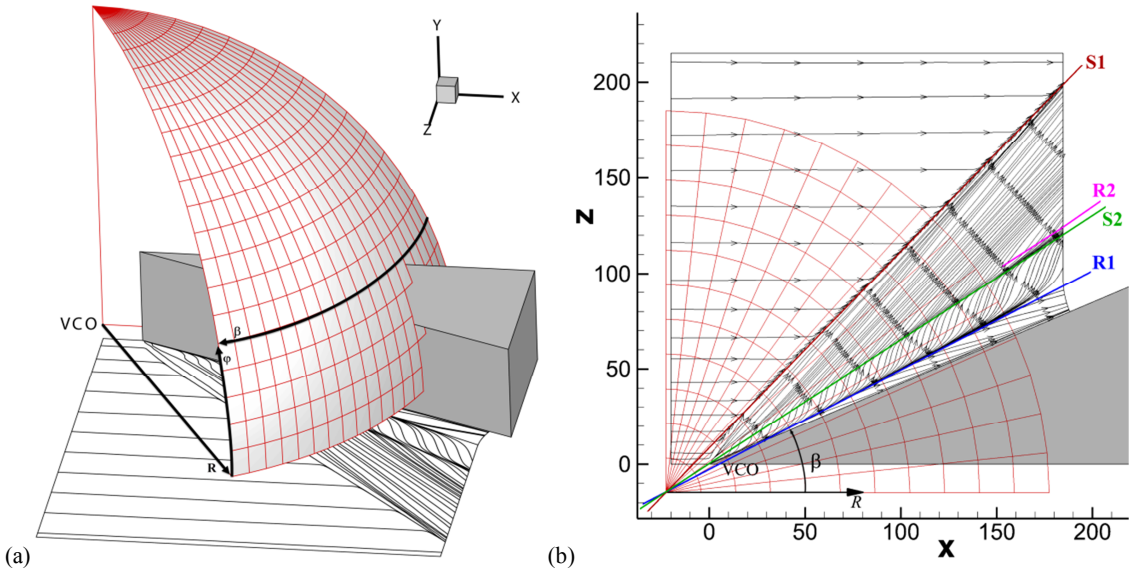

Figure 7 Sketch of (a) the VCO coordinate system, and (b) the projection of (a) onto the bottom wall. Line R2 is acquired via the pressure field.

The shock-wave system is visualized by using density gradient based numerical Schlieren [64] and pressure gradient magnitude $|\nabla p| = \sqrt{\frac{\partial p}{\partial x_i}\frac{\partial p}{\partial x_i}}$ at the cross-section of $R = 226.3mm$ in Figure 8, from which we can see clearly the λ-shock-wave system, which is composed of the main shock-wave, the front shock-wave (i.e. separation shock-wave) and the rear shock-wave (i.e. reattachment shock-wave), respectively. The boundary layer separates at S1 while interacting with the front shock-wave and a separated free shear-layer can be seen as the strong fluctuation of the density gradient. The rear and the front shock-wave legs meet the main shock-wave at the "triple point", and the rear shock-wave is stronger than the front shock-wave. A slip line is emitted from the triple points and a jet-like flow bounded by the slip line is then formed. The "jet" turns around the separation vortex and impinges onto the wall near the mean reattachment line R1. At the impingement location, part of the jet penetrates the separation vortex and forms the reverse flow, which is in agreement with the physical model proposed by Alvi and Settles [65]. Two separated regions with shocklets can be identified in the jet flow. Firstly, some shocklets can be observed between the rear shock-wave and the slip line, and whilst the turning of the jet is accomplished via a Prandtl-Meyer expansion fan, therefore, the shocklets are suppressed in this region. Further downstream, the expansion fan reflects from the slip line as compression waves, which coalesce and form shocklets and finally the shocklet becomes a normal shock-wave that terminates the supersonic jet prior to its impingement to the wall. The expansion waves and the shocklets can be seen more clearly from the contours of $|\nabla p|$. From Figure 8 (b), some shocklets can also be found beneath the front and the rear shock-waves and also in the reverse flow region. The shocklets beneath the

front and the rear shock-waves will coalesce onto the front and the rear shock-wave, which is the same as the process seen in the two dimensional SWTBLI [29,64]. The shocklets in the reverse flow locate near S2-R2, which are mainly responsible for the secondary flow separation.

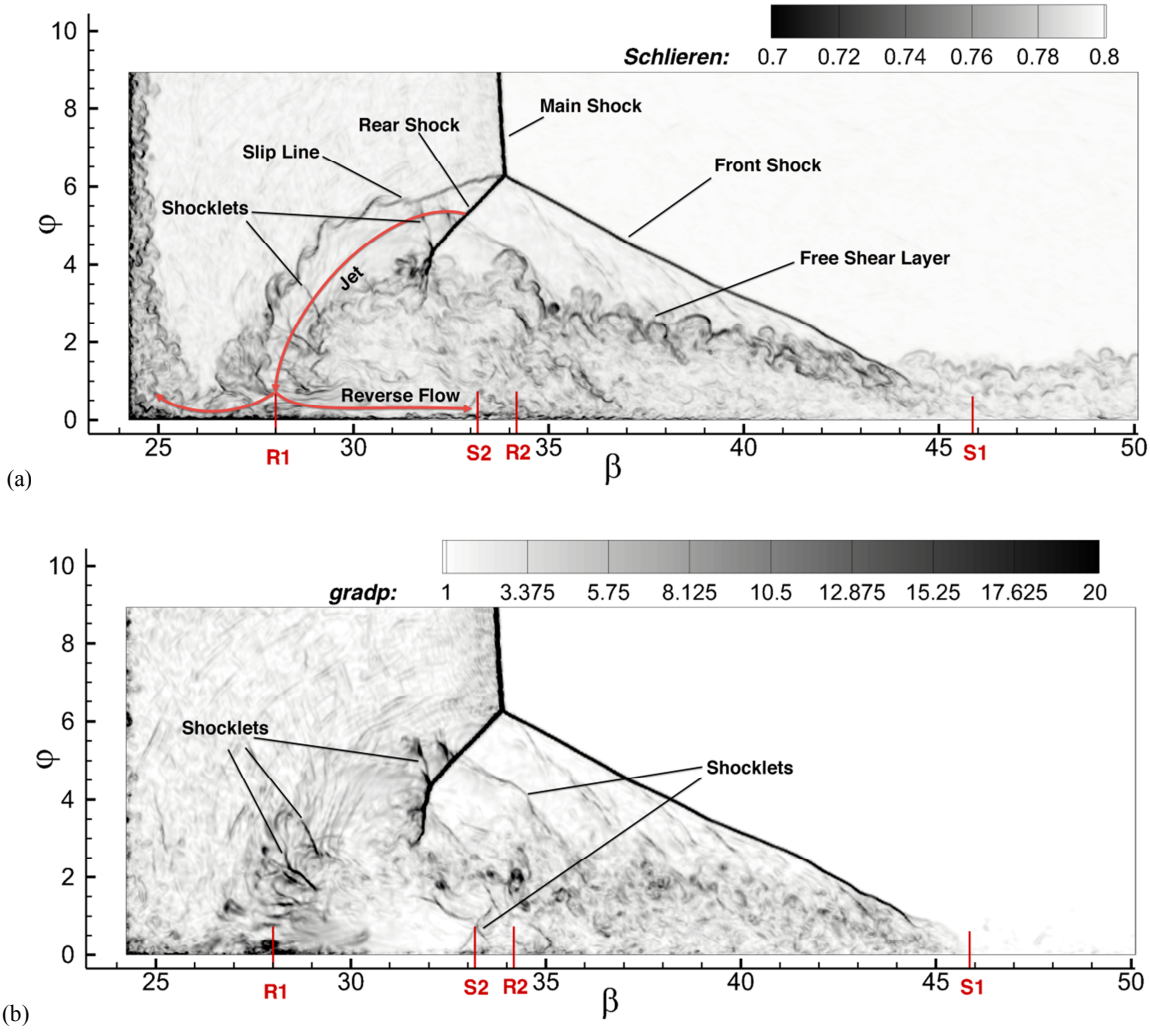

Figure 8 Instantaneous numerical Schlieren (a) and pressure gradient magnitude (b) on the 3D spherical arc section of $R = 226.3$ mm

The instantaneous 3D shock-wave structure is visualized by using an iso-surface of $|\nabla p|$ as shown in Figure 9. From the figure we can see that, the main shock-wave is basically a 2D planar surface as expected. The front shock-wave, however, presents some three-dimensional wrinkles. Small-scale wrinkles can be seen near the foot of the separation shock-wave and large-scale wrinkles are observed in the outer part of the front shock-wave. This can be explained by the interaction between the front shock-wave and the turbulence structures in the incoming boundary layer, in which the length scale of the latter increases with the distance from the wall. Similar phenomena were also reported in other forms of shock-wave/turbulence interactions. [58, 64, 66] By extending the triple point line and the line

of the shock-wave foot, we can see that, the two lines intersect at the VCO location, which again validates the quasi-conical characteristics of the shock-wave system.

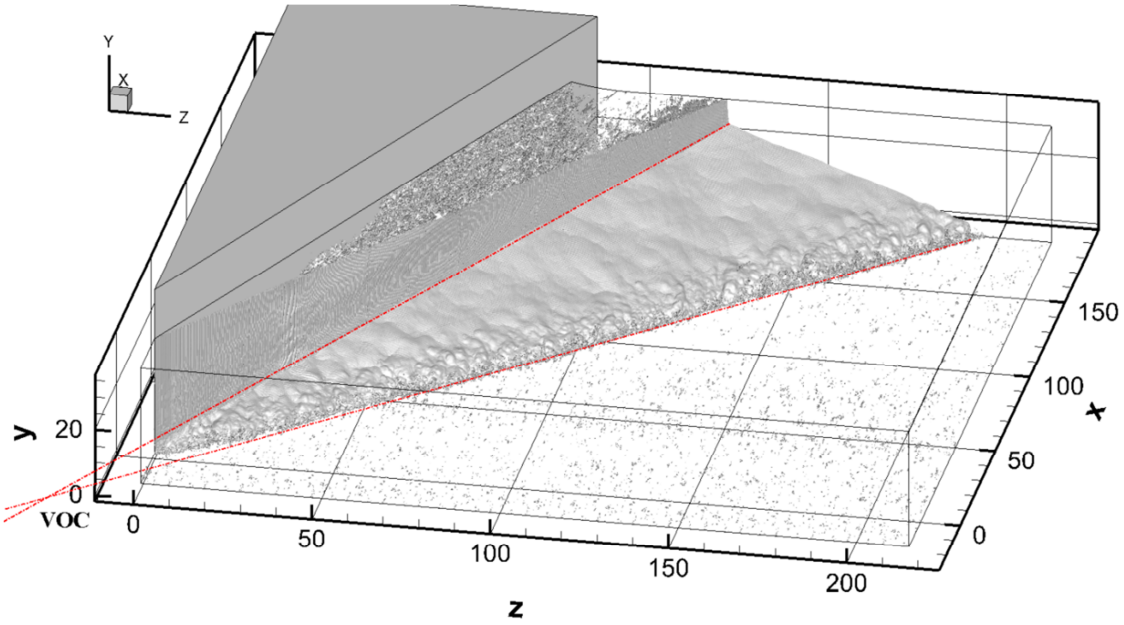

Figure 9 Instantaneous shock-wave surface visualized by using the iso-surface of the pressure gradient magnitude $|\nabla p| = 5\, p_0/\delta_0$

C. Separation Structures

According to the mean skin-friction-line (or wall limiting streamline at the bottom wall in Figure 7 b), we can clearly see the main flow separation line S1, the reattachment line R1 and the secondary separation line S2. The secondary reattachment R2 can also be hazily identified and it can be also surmised from the wall pressure distribution in Figure 6 (a). Therefore, the pattern of wall streamlines of the present case is coincident with that of the regime VI in the regime map of Zheltovodov et al. [9,15] at the same Mach number and deflection angle.

The skin-friction-lines at the surface of the fin are demonstrated in Figure 10, from which we can see the streamlines converge to the separation line S3 near the bottom of the fin surface. Very close to the fin's root, a divergence line marked with R3 can be further observed, as shown in Figure 10 (b). The convergence and divergence lines at the surface of the fin can also be found in the experimental oil-flow visualization by Zheltovodov[15] as described by Zheltovodov and Knight[20] in the same flow regime, which indicates the existence of a longitudinal corner separation vortex.

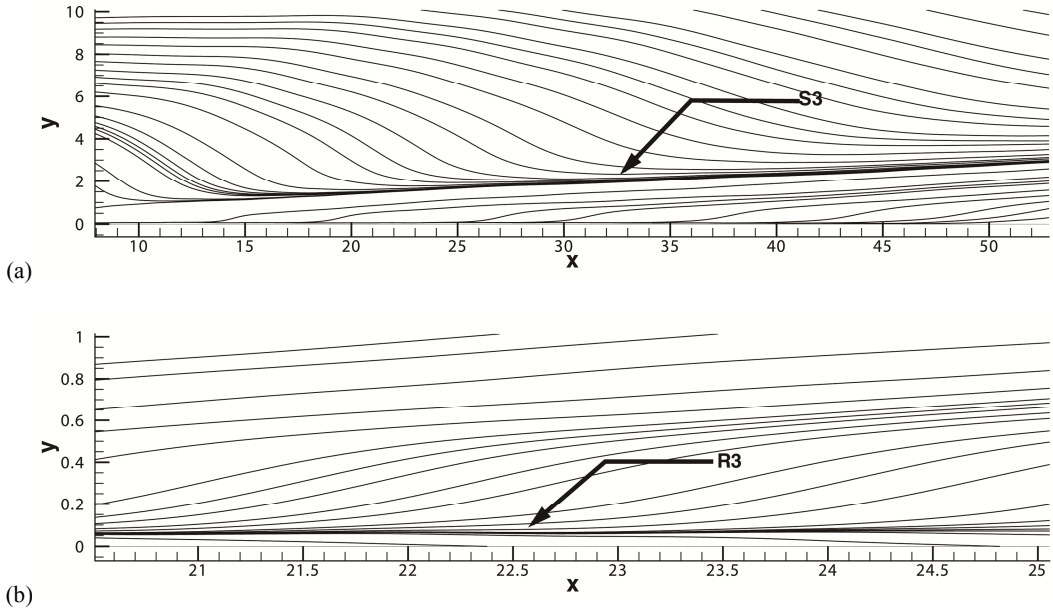

Figure 10 Mean skin-friction-line at the surface of the fin (a). The near-wall region is zoomed out in (b)

The streamlines (u_β, u_φ) on the 3D spherical arc section of *R*=226.3 mm are presented in Figure 11. Unlike the closed configuration of the streamlines seen in a 2D separation bubble, the streamlines in Figure 11 spiral around two foci where they eventually disappear, presenting the 3D characteristics of the flow separation. The two foci are in fact the main separation vortex core and the corner vortex core, respectively.

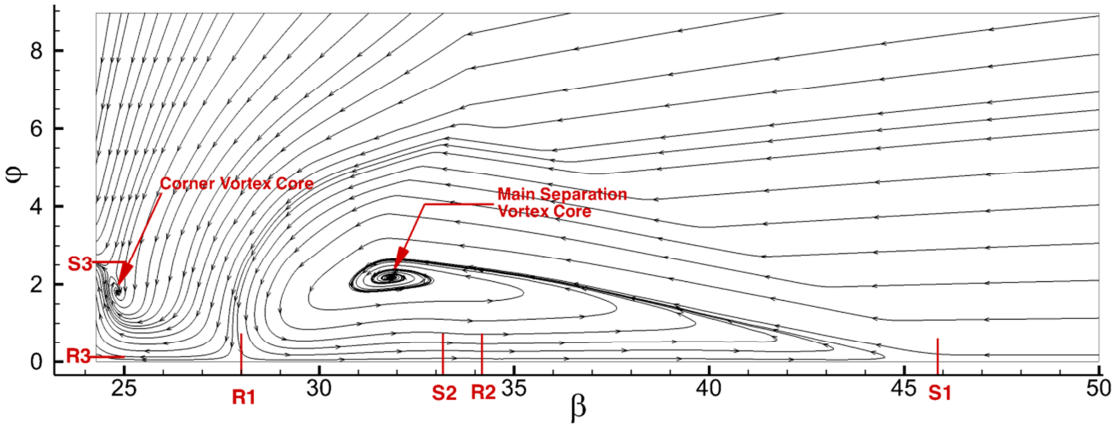

Figure 11 Mean streamlines (u_β, u_φ) on a 3D spherical arc section of $R = 226.3$mm.

The streamlines originating from different *y*-positions at the inlet plane are shown in Figure 12. It can be seen that the streamlines of different layers present different structures and patterns. The streamlines at the near-wall layer *y*=2 mm ($0.5\delta_0$, see Figure 12 a) presents a spiral structure around the separation vortex core. At a higher layer *y*=4 mm ($1\delta_0$, see Figure 12 b), the streamlines may directly enter the reversal flow region, rather than go through

the vortex core. Further increasing the layer's height to y=6 mm (1.6δ_0, see Figure 12 c), part of the streamlines go into the reverse flow and the other part goes towards the corner region, indicating the existence of the corner vortex. The streamlines at the top layer y=10 mm (2.6δ_0, see Figure 12 d) do not reverse and they directly impinge onto the mean reattachment line R1 and then move towards the surface of the fin.δ_0

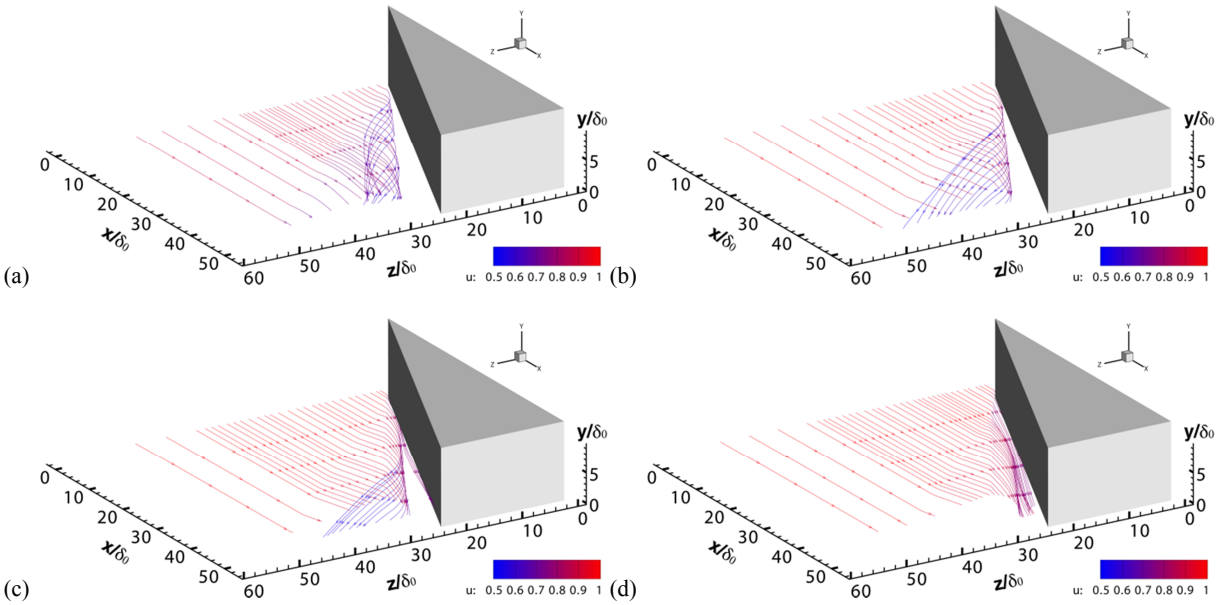

Figure 12 Streamlines originating from y=0.5δ_0 (a), y=δ_0 (b), y=1.6δ_0 (c) and y=2.6δ_0 (d) on the inlet plane. The color represents for $\langle u \rangle$

The streamlines in the corner region are zoomed in Figure 13, in which the helical streamlines indicating the existence of the corner vortex can be clearly seen. The corner vortex originates near the leading edge of the fin's surface. Further downstream, the fluid inside the corner vortex will have an increased speed, which can be attributed to the strong sweeping events caused by the flow impinging towards the corner region.

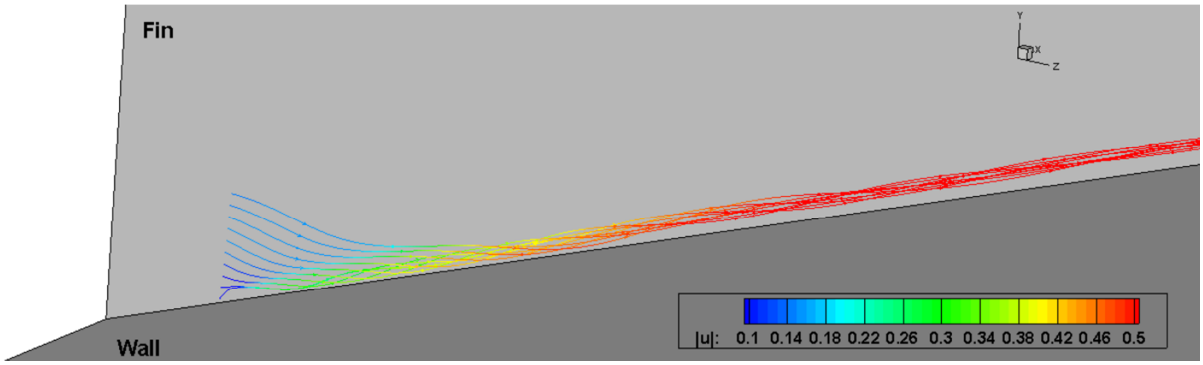

Figure 13 Streamlines in the corner region, with the color of the velocity magnitude $|\langle \vec{u} \rangle|$.

D. Mean Flow Field

The mean density field, mean stagnation pressure, static pressure and conical-cross Mach number M_n are presented in Figure 14. The main flow features including the shock-wave structures, the separation vortex, and the separation shear-layer can be identified as 1, 2, 3 and 4, respectively in the mean density field, and are consistent with the experimental observation of Hsu and Settles [67]. From the mean stagnation pressure in Figure 14 (b), we can see the jet flow with a high level of stagnation pressure wrapping around the vortex core. The jet is supersonic initially and undergoes further acceleration during the expansion process. The supersonic jet is finally terminated after a normal shock-wave (as seen in Figure 8) and then it penetrates underneath the main vortex into the near-wall separation region and gets accelerated to supersonic speed again (Figure 14 d). Near the impinging location R1, the density and the pressure increase significantly (Figure 14 c), and the high pressure drives the flow towards both sides of R1. Near the secondary separation line S2, an adverse pressure gradient can be seen, which can be attributed to the shocklets and the normal shock-wave in this region (as shown in Figure 8 c). The adverse pressure gradient could be the reason for the secondary flow separation.

The penetration of the jet brings high momentum fluid into the near-wall reverse flow region and is responsible for the energetic turbulence in the reverse flow layer. Such a mechanism is clearly missing in a 2D SWTBLI, therefore, the reverse flow in a 2D flow separation is usually quiescent and less organized, often referred to as the dead zone.

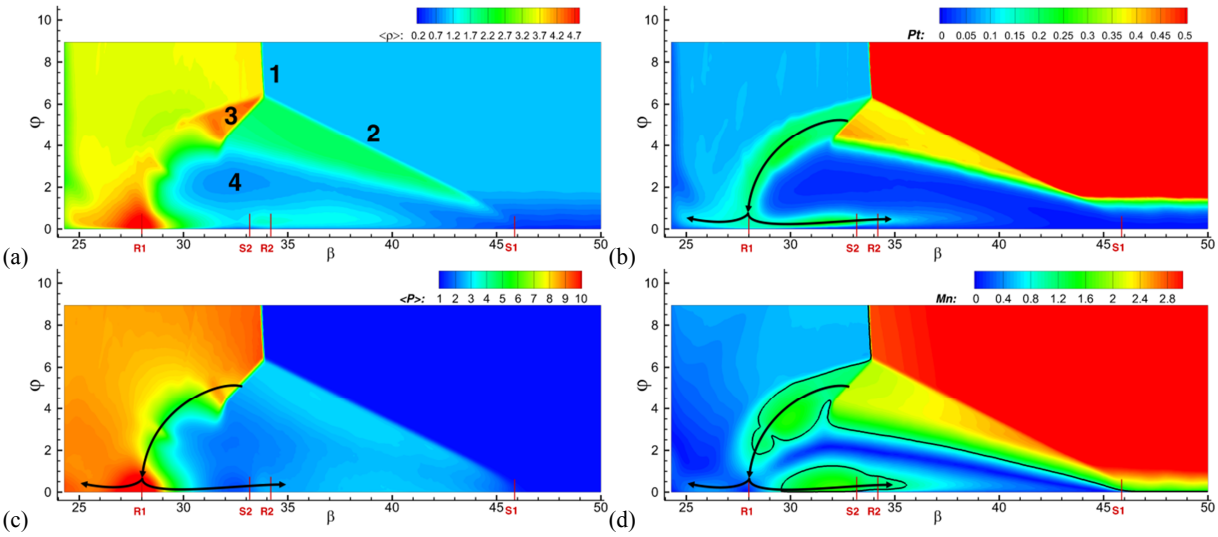

Figure 14 Distributions of (a) mean density field, (b) the stagnation pressure, (c) the static pressure, and (d) the conical cross Mach number M_n , on the section of $R = 226.3$mm. The black thin line in (d) denotes the contour with $M_n = 1$. All variables except M_n are normalized with their free-stream incoming values

The mean shear strength, which can be measured with the vorticity magnitude as $\Omega = \sqrt{\langle \Omega_i \Omega_i \rangle}$, is shown in Figure 15, from which we can see that, regardless of the near-wall region, the strong shear region includes the free-shear-layer induced by the main flow separation and the slip line. The shear strength in the center of the jet is low, which can be seen as a common characteristic of the jet flow. In the core of the reverse flow, lower shear strength follows as a gap between the free shear-layer and the near-wall layer.

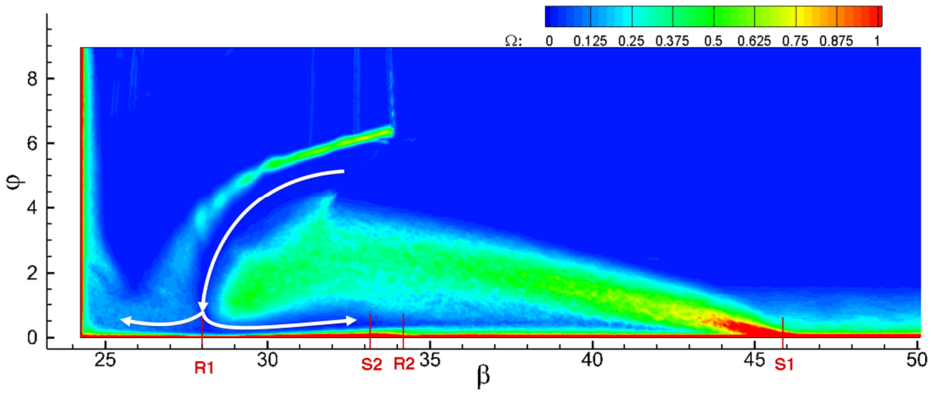

Figure 15 Distributions of the mean vorticity strength Ω on the section of $R = 226.3$mm. Ω is normalized by u_0/δ_0.

E. Turbulence Field

An analysis of the instantaneous flow field was performed to explore the turbulence characteristics. Figure 16 shows the instantaneous streamwise velocity fluctuations u_s'' in the near-wall $x-z$ plane at $y = 0.085$mm (i.e. $y^+ = 10$ at the inlet plane). u_s'' is defined as,

$$u_s'' = \vec{u}'' \cdot \vec{n}, \tag{3}$$

where $\vec{u}'' = (u'', v'', w'')^T$ is the vector of the velocity fluctuation and $\vec{n} = \langle \vec{u} \rangle / |\langle \vec{u} \rangle|$ is the unit vector of the mean flow.

Upstream of the interaction zone, classic *x*-direction elongated streaky structures can be found in the undisturbed boundary layer. Near the separation line (see Figure 16 c), the streaks are distorted and their scales is decreased, which indicates the activation of the near-wall turbulence by the adverse pressure gradient (APG) caused by the interaction with the front shock-wave. This kind of modification of the near-wall coherent structures has also been observed in 2D SWTBLI with flow separation [58,68]. In the near-wall region beneath the main separation zone, energetic streaky structures can also be seen, but they are rearranged in the direction of the skin-friction lines, which means the wall turbulence like structures (quasi-streamwise vortices) are rapidly regenerated in the separation zone.

This is quite different to the 2D flow separations, in which the regeneration of the wall turbulence happens downstream of the reattachment location and the flow in the separation zone often lacks organized turbulent flow structures [68].

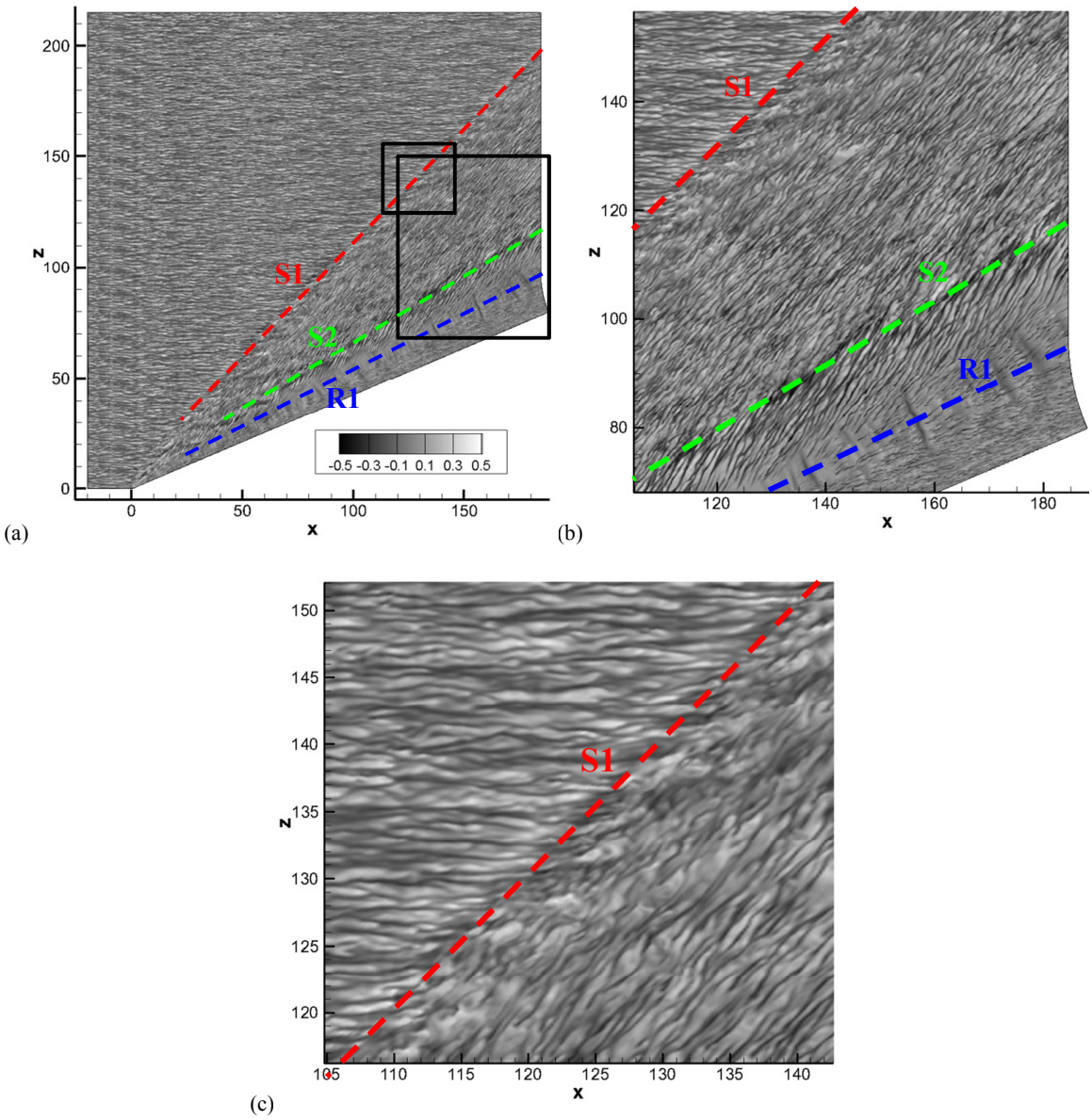

Figure 16 Instantaneous fields of u_s'' at $y = 0.085$ mm. The squared regions in (a) are zoomed in (b) and (c).

It is inferred that the jet flow originating from the external flow brings high kinetic energy fluids to the near-wall region and that the local pressure gradient further drives high energy fluids to the near-wall region in the separation zone of the reverse flow (as presented in Figure 14). Consequently, the near-wall flow has high kinetic energy and large fluctuations which promote the "fast" flow transition to turbulent status in a very short distance. The transition

process can be seen in Figure 16 (b), in which a small region around R1 has less organized structures. This region is the location where the jet impinges and the turbulent flow is not yet fully organized. At both sides of line R1, the streaky structures are regenerated, indicating the regeneration of the wall turbulence.

Near the line S2, we can see the streaks are distorted and activated by APG again, which is similar to the process of the main flow separation. This provides evidence that the secondary separation in the present flow is essentially a turbulent separation.

The velocity fluctuations at two planes (y = 1.32 *mm* and 8.15 *mm*), which cross the low-shear region and the main separation vortex, are presented in Figure 17. In the undisturbed boundary layer, the velocity fluctuation at y = 1.32 mm is weaker and has a larger length scale than those in the near-wall region (as shown in Figure 16 a), which can be attributed to the ejection of low-energy fluid via the large-scale hairpin vortex head in the boundary layer.[69] Near the front shock-wave, the fluctuations are largely amplified, due to the interaction with the front shock-wave. In the core of the reverse jet, the flow exhibits fewer fluctuations and is less organized. For the slice at y = 8.15mm (about $2\delta_0$), the flow upstream of the shock-wave is almost inviscid, however, inside the interaction zone, strong fluctuations can be seen. These fluctuations are driven by the large-scale turbulence structures in the detached free shear-layer of the main flow separation.

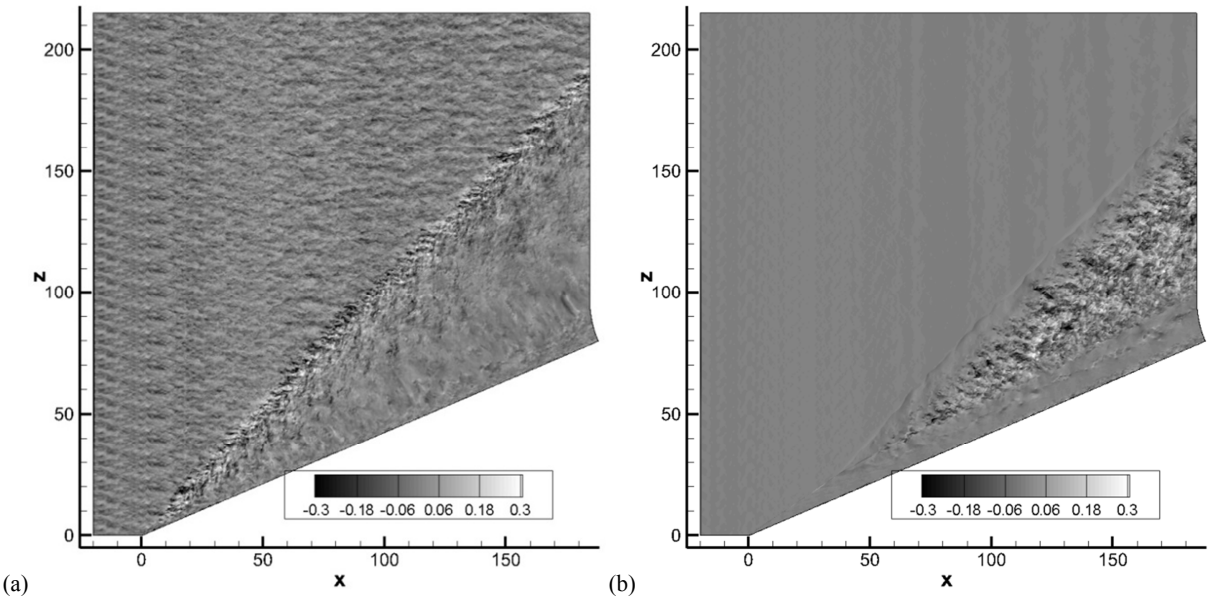

Figure 17 Instantaneous fields of u_s'' at (a) y=1.32 mm and (b) y= 8.15 mm.

From the instantaneous fluctuation u_R'' on the 3D spherical arc section of $R = 226.3$ mm shown in Figure 18, the turbulent structures are further investigated. Five zones can be distinguished according to different

characteristics of turbulent flow structures. The first zone includes the undisturbed boundary layer attached to the bottom wall and the side-wall surface of the fin, where the turbulent flow structures are the classic quasi-streamwise hairpin vortices attached to the wall [69]. The second zone is the separated free-shear-layer zone, in which the turbulence contains some large-scale structures detached from the wall with a high level of turbulent kinetic energy. The turbulent flow structures in this zone are similar to those seen in the mixing layer, in which the flow is also dominated by the free shear-layer [70]. The third zone is at the edge of the jet, in which the flow is also dominated by the free shear-layer flow. The difference between this zone and the second zone is that, the jet flow is not yet developed to a fully turbulent state in its beginning part. Therefore, we can observe the transition process and the generation of large-scale structures due to the Kelvin–Helmholtz instability along the shear-layer, as shown in the instantaneous Schlieren image in Figure 8. The fourth zone is in the reverse flow, where some quasi-streamwise structures exit. The flow structures in this zone are similar to the wall turbulence seen in the first zone, but the structures are confined within a thin layer close to the wall, therefore, no large-scale structures, such as the hairpin vortex heads, can be located. The fifth zone is the low-turbulence zone, which includes the core of the jet and a gap between the second zone and the fourth zone.

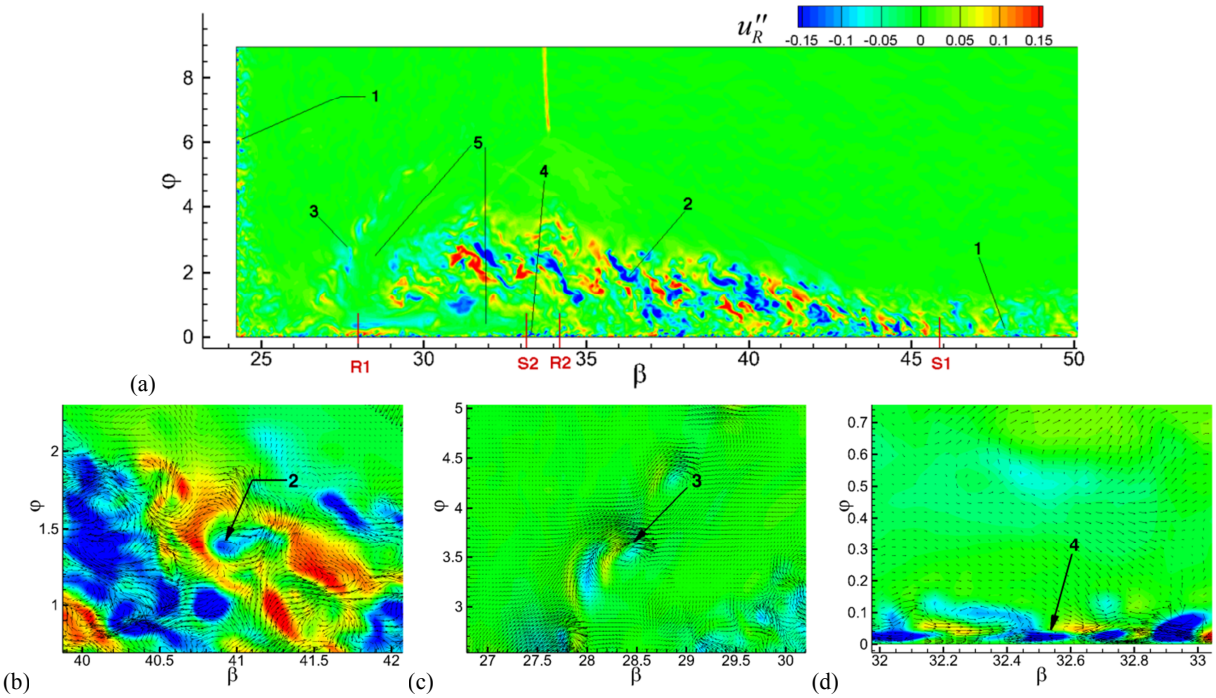

Figure 18 Instantaneous u_R'' on the section of $R = 226.3$mm (a). (b), (c) and (d) are the detail images of local flow structures in (a). The arrow stands for the 2D vector of (u_β'', u_φ''). Labels 1-5 indicate the five identified zone respectively.

The vorticity fluctuation in the R direction $\Omega_R{}''$ on the cross section of $R = 226.3$ mm are presented in Figure 19, in which $\Omega_R{}''$ is normalized by u_0/δ_0. Since the vorticity and the swirling strength are closely related to the vortical structures, the above mentioned five zones can be more easily distinguished in Figure 19.

The structures in zone 1 are the combination of small-scale strong fluctuations in the near-wall region and large-scale weaker fluctuations in the outer-layer. The turbulence level in zone 2 is also very strong, but these fluctuations are weakened due to the diffusion of the free-shear-layer. Zone 3 only occupies a slender region, in which the transition of the free shear-layer due to the Kelvin–Helmholtz instability can be seen. Zone 4 is a thin layer attached to the wall, but its fluctuations are strong. Zone 5 presents a gap between zone 2 and zone 4. The transition process can be seen in zone 3. The intensity of the flow structures in zone 3 increases with the development of the jet flow, and finally these structures enter the corner region and the reverse flow after the impingement of the jet.

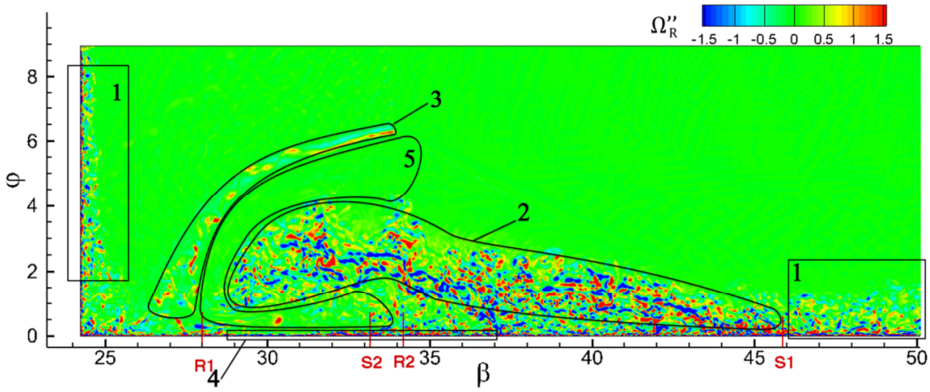

Figure 19 Instantaneous field of vorticity fluctuation $\Omega_R{}''$ on the section of $R = 226.3$mm.

The iso-surface of the swirling strength λ_{ci} [71] is used to visualize the Turbulent coherent structures in Figure 20. Firstly, the quasi-streamwise vortex in zone 1 can be clearly identified as the typical quasi-streamwise wall turbulence in Figure 20 (a). In the interaction zone, the most significant phenomenon is the amplification of the turbulence in the free shear-layer (zone 2). With close observation of the shear-layer in Figure 20 (c), large-scale detached coherent structures and the low turbulence tone beneath the free shear-layer can be clearly seen. Figure 20 (d) highlights the coherent structures in zone 3 by using a smaller value for the iso-surface ($\lambda_{ci} = 0.02\%\,\lambda_{ci,max}$). From this figure, we can see some large-scale structures are generated within the transition of the jet and theses structures are amplified after interaction with the normal shock-wave just before its impingement onto the wall, similar to the shock-wave/free turbulence interaction.[35,66] To identify coherent structures in the reverse flow, the near-wall part of the domain $y^+ < 50$ is displayed in Figure 20 (b), from which we can see massive streamwise

elongated coherent structures aligned in the direction of the skin-friction-line. These structures are similar to those quasi-streamwise vortices seen in the incoming undisturbed boundary layer, therefore it can be regarded as a kind of wall turbulence like coherent structures.

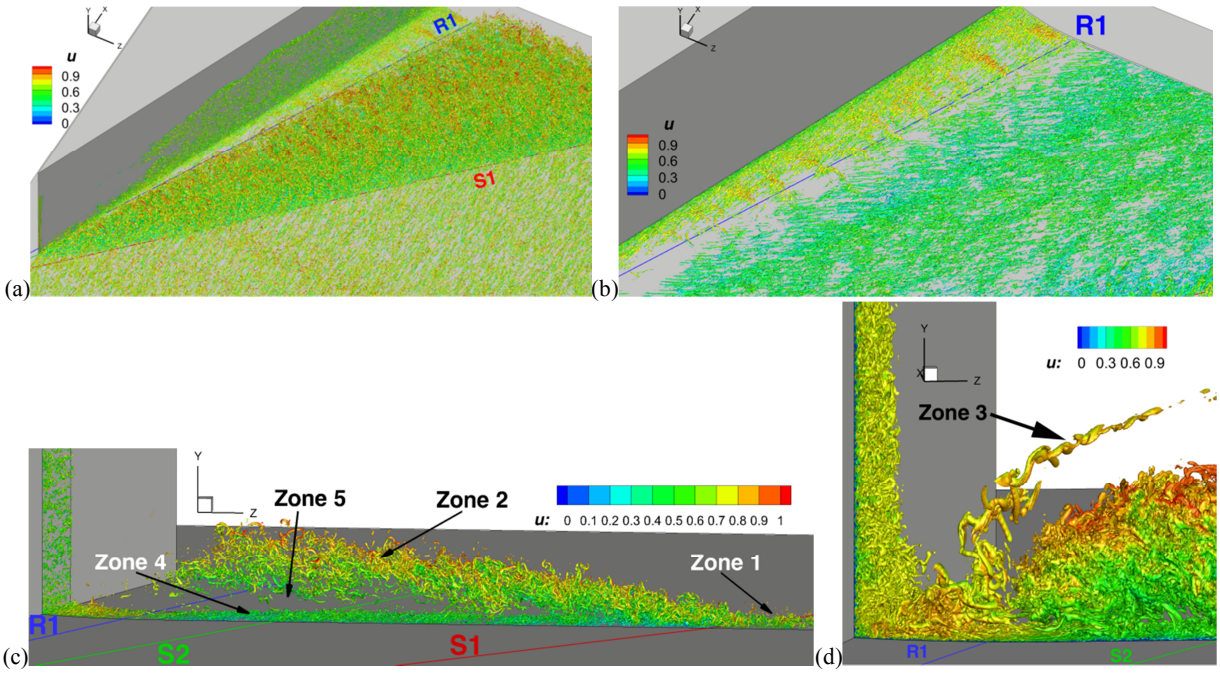

Figure 20 Turbulent coherent structures visualized using iso-surface of λ_{ci} equaling 0.3% of its global maximum, colored by the instantaneous u-velocity; (b) presents the near-wall region of y<0.5 mm; (c) highlights the region of $160 < x < 170$; (d) further highlights the region around the jet with λ_{ci} equaling to 0.02% $\lambda_{ci,max}$.

The turbulent kinetic energy (TKE) $K = \frac{1}{2}(\langle u''u'' \rangle + \langle v''v'' \rangle + \langle w''w'' \rangle)$ on the $R = 226.3$mm section is presented in Figure 21. Consistent with the previous analysis, TKE values are high in zone 2. At the edge of the jet of zone 3, the level of TKE increases during the transition of the jet shear-layer. In the reverse flow, a thin layer with high TKE can be seen in the detail Figure 21 (b), and the TKE is further amplified around the line S2. The amplification mechanism is similar to that around the line S1, possibly due to the activation of wall turbulence by APG. However, the amplification of turbulence at line S_2 is confined within a thin layer, therefore, no large-scale detached free-shear-layer can be observed. Again, this proves that the near-wall reverse flow is essentially turbulent and the secondary separation at S2 is a turbulent separation.

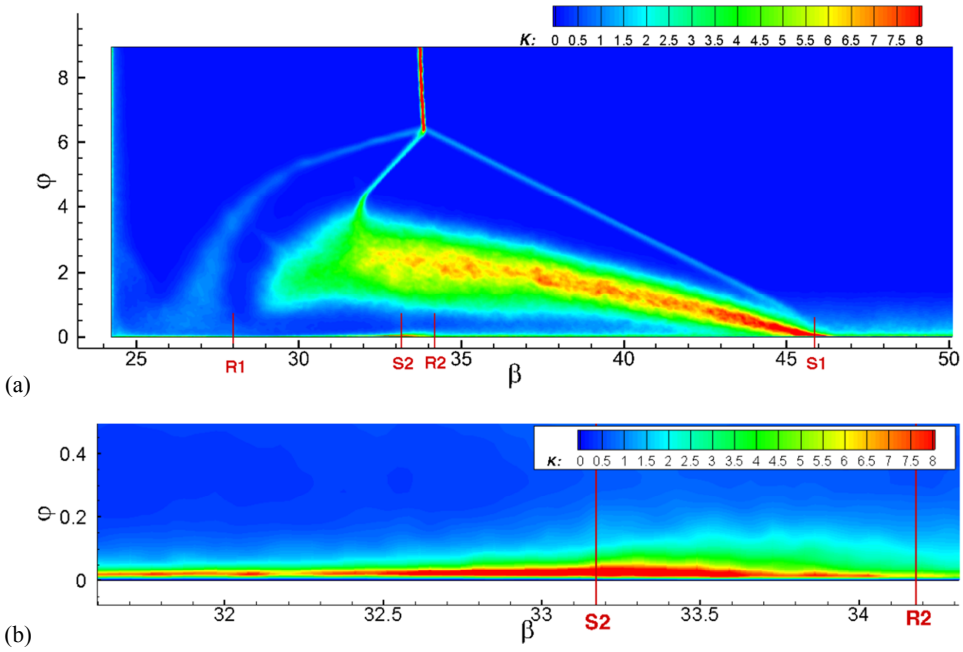

Figure 21 Turbulent kinetic energy on the section of $R = 226.3$mm, normalized by the square of the wall friction velocity u_τ^2 at the inlet.

IV. Conclusions

The 3D SWTBLI of a hypersonic flow passing a sharp 23° single-fin mounted on a flat plate at Mach 5 has been investigated in the present work by using LES. The results demonstrate good agreement with available experimental data in terms of the mean flow field structure, the surface pressure distributions as well as the surface flow patterns. However, significant under-prediction in the surface skin-friction peak in the vicinity of the primary reattachment line is observed. The specification of possible reasons for such a discrepancy as well as the analysis of surface heat transfer prediction is important and will be analyzed at the next stage of the research.

The LES data are analyzed to investigate flow properties and the turbulence characteristics. It is demonstrated that an unsteady λ-shock-wave system is formed in the 3D SWTBLI. Wrinkling of the front shock-wave surface was observed, which is caused by the interaction with turbulence structures in the incoming boundary layer and the scale of such wrinkles increases with distance from the wall.

The flow is separated at the foot of the separation shock-wave and reattaches near the corner region. The secondary flow separation and reattachment lines can also be identified, which is consistent with the characteristic regime VI suggested by Zheltovodov et al. [9,15,16]. The streamlines lift-off at the separation line and return back near the fin's surface, which transports high momentum fluid to the near-wall region. In the separation vortex region, the

streamlines curl around the separation vortex core and reverse flow is generated beneath the separation vortex. The helical streamlines in the corner region indicate the existence of the corner vortex.

The flow field of the 3D single-fin can be categorized into five different zones according to the characteristics of the turbulent flow structures. Zone 1 is the undisturbed wall turbulence in the upstream boundary layer. Zone 2 is the separated free shear-layer, which contains large-scale unsteady structures. Zone 3 is near the slip line at the edge of the jet. The turbulence in this zone is also dominated by the free shear but the flow is still in the process of transition. Zone 4 is the reverse flow, which is also characterized by the wall-turbulence, but confined in a thin layer attached to the wall. Zone 5 is the low-turbulence zone, which includes the core of the jet and the gap between zone 2 and zone 4.

The analysis of the turbulent flow field supports the experimental observation that the near-wall reverse flow beneath the main separation vortex in Regime VI is fully turbulent and the secondary separation is essentially a turbulent separation. The transition to turbulence in the reverse flow happens within a short distance from the impinging location of the jet flow at the primary reattachment line R1, mainly due to the strong kinetic energy contained in the jet flow.

Acknowledgments

This work is supported by the National Natural Science Foundation of China (Nos. 11302012, 11572025, 51420105008 and 51476004), the Leverhulme trust of UK (No. CE-12-10050002), and the National Basic Research Program of China (No. 2012CB720205). Computer time for the present study was provided via the UK Turbulence Consortium (EPSRC Grant No. EP/L000261/1) and the simulations were run on the UK High Performance Computing Service ARCHER. The second author (Y. Yao) would like to acknowledge the Zhejiang Provincial 1000 HaiOu scheme in supporting his research visits to Zhejiang University, P.R. China.

References

[1] Dolling, D. S., “Fifty Years of Shock-Wave/Boundary-Layer Interaction Research: What Next?” *AIAA Journal*, Vol. 39, No. 8, 2001, pp. 1517–1531.

[2] Gaitonde, D. V., "Progress in Shock Wave/Boundary Layer Interactions." *Progress in Aerospace Sciences*, Vol. 72, 2015, pp. 80–99.

[3] Knight, D., Yan, H., Panaras, A. G., and Zheltovodov, A., “Advances in CFD Prediction of Shock Wave Turbulent Boundary Layer Interactions,” *Progress in Aerospace Sciences*, Vol. 39, 2003, pp. 121–184.

[4] Panaras, A. G., "Review of the Physics of Swept-Shock/Boundary Layer Interactions." *Progress in Aerospace Sciences*, Vol. 32, 1996, pp. 173-244.

[5] Token, K., "Heat Transfer Due to the Shock-Wave/Turbulent-Boundary-Layer Interactions on High Speed Weapons Systems," Air Force Flight Dynamics Laboratory, AFFDL-TR-74-77, 1974.

[6] Settles, G. S., “Swept Shock/Boundary-Layer Interactions: Scaling Laws, Flowfield Structure, and Experimental Methods, Special Course on Shock-Wave/Boundary-Layer Interactions in Supersonic And Hypersonic Flows,” AGARD Report, 762, 1993, 1-1–1-40.

[7] Zheltovodov, A. A., and Schülein, E., “Three-Dimensional Swept Shock Waves/Turbulent Boundary Layer Interaction in Angle Configurations,” Preprint No. 34–86, ITAM, USSR Academy of Sciences, Novosibirsk, 49, 1986 (in Russian)

[8] Zheltovodov, A. A., Dvorak, R., and Safarik, P., “Shock waves/turbulent boundary layer interaction properties at transonic and supersonic speeds conditions. *Izvestiya SO AN SSSR, Seriya Tekhnicheskih Nauk* (*Proceedings of the USSR Academy of Sciences, Siberian Branch, Series of Technical Sciences*), 6 (1990), 31–42 (in Russian)

[9] Zheltovodov, A. A., “Some Advances In Research of Shock Wave Turbulent Boundary-Layer Interactions,” *44th AIAA Aerospace Sciences Meeting and Exhibit*, 2006, AIAA Paper 2006–0496.

[10] Schülein, E., and Zheltovodov, A. A., “Documentation of Experimental Data for Hypersonic 3-D Shock Waves/Turbulent Boundary Layer Interaction Flows,” DLR Internal Report, IB 223–99 A 26, 95 (2001).

[11] Kubota, H., and Stollery, J. L., “An Experimental Study of the Interaction between A Glancing Shock and A Turbulent Boundary Layer,” *Journal of Fluid Mechanics*, Vol. 116, 1982, pp. 431–58.

[12] Zubin, M., and Ostapenko, N., “Structure of Flow in the Separation Region Resulting from Interaction of a Normal Shock Wave with a Boundary Layer in a Corner,” *Fluid Dynamics*, Vol. 14, Issue 3, 1979, pp. 365-371.

[13] Zubin, M. A., and Ostapenko, N. A., “Geometrical Characteristics of the Separation of a Turbulent Boundary Layer in the Case of Interaction with a Normal shock Wave in a Conical Flow,” *Fluid Dynamics*, Vol. 18, Issue 6, 1983, pp. 167–875.

[14] Dem’yanenko V.S., and Igumnov V.A., “Spatial Shock Wave-Turbulent Boundary Layer Interactions in the Interference Region of Intersecting Surfaces,” *Izvestiya SO AN SSSR, Seriya Tehnicheskih Nauk* (*Proceedings of the USSR Academy of Sciences, Siberian Branch, Series of Technical Sciences*), No. 2, 1975, pp. 56–62 (in Russian).

[15] Zheltovodov, A., “Regimes and Properties of Three-Dimensional Separation Flows Initiated by Skewed Compression Shocks,” *Journal of Applied Mechanics and Technical Physics*, Vol. 23, No. 3, 1982, pp. 413–418.

[16] Zheltovodov, A., Maksimov, A., and Schülein, E., “Development of Turbulent Separated Flows in the Vicinity of Swept Shock Waves.” The Interactions of Complex 3-D Flows, edited by A. Kharitonov. Novosibirsk, 1987, pp. 67–91 (in Russian).

[17] Zheltovodov, A. A., "Shock Waves/Turbulent Boundary-Layer Interactions: Fundamental Studies and Applications." 1996, AIAA Paper 96–1977.

[18] Settles, G. S., and Dolling, D.S., "Swept Shock/Boundary-Layer Interactions, Tutorial and Update," 28th Aerospace Sciences Meeting, AIAA Paper 90-0375.

[19] Bogdonoff, S. M., "Flowfield Modeling of a Three-Dimensional Shock Wave Turbulent Boundary Layer Interaction," Springer-Verlag Berlin Heidelberg, Novosibirsk, USSR, 1991, pp. 279-302.

[20] Zheltovodov, A. A., and Knight, D. D., "Ideal Gas Shock Wave-Turbulent Boundary-Layer Interactions in Supersonic Flows and Their Modeling: Three-Dimensional Interactions,” edited by H. Babinsky and J. Harvey, Cambridge University Press, New York, 2011, pp. 202–258.

[21] Knight, D., “Numerical Simulation of 3-D Shock Wave Turbulent Boundary Layer Interactions,” AGARD-R-792, Paper 3, 1993.

[22] Kim, K., Lee, Y., Alvi, F., Settles, G., and Horstman, C., "Skin Friction Measurements and Computational Comparison of Swept Shock Boundary Layer Interactions," *AIAA Journal*, Vol. 29, No. 10, 1991, pp. 1643–1650.
[23] Liu, Y., Yu, X., and Liu, B., "Turbulence Models Assessment for Large-Scale Tip Vortices in an Axial Compressor Rotor", *Journal of Propulsion and Power*, Vol. 24, No. 1, 2008, pp. 15-25.
[24] Panaras, A. G., "The Effect of the Structure of Swept Shock-Wave/Turbulent Boundary-Layer Interactions on Turbulence Modeling," DLR-IB 223-96 A 21; German Aerospace Center (DLR): Köln, Germany, 1996.
[25] Panaras, A.G., "The Effect of the Structure of Swept-Shock-Wave/Turbulent-Boundary-layer Interactions on Turbulence Modelling", *Journal of Fluid Mechanics*, Vol. 338, 1997, pp. 203-230.
[26] Panaras, A. G., "Turbulence Modeling of Flows with Extensive Crossflow Separation," *Aerospace*, Vol. 2, 2015, pp. 461-481.
[27] Urbin, G., and Knight, D., "Large-Eddy Simulation of a Supersonic Boundary Layer Using an Unstructured Grid," *AIAA Journal*, Vol. 39, No. 7, 2001, pp. 1288-1295.
[28] Kaenel, R., Kleiser, L., Adams, N. A., and Vos, J. B., "Large-Eddy Simulation of Shock-Turbulence Interaction," *AIAA Journal*, Vol. 42, No. 12, 2004, pp. 2516-2528.
[29] Loginov, M. S., Adams, N. A., and Zheltovodov, A. A., "Large-Eddy Simulation of Shock-Wave/Turbulent-Boundary-Layer Interaction," *Journal of Fluid Mechanics*, Vol. 565, 2006, pp. 135-169.
[30] Touber, E. and Sandham, N. D. "Large-Eddy Simulation of Low-Frequency Unsteadiness in a Turbulent Shock-Induced Separation Bubble," *Theoretical and Computational Fluid Dynamics*, Vol. 23, No. 2, 2009, pp. 79-107.
[31] Wang, B., Sandham, N. D., Hu, Z., and Liu, W., "Numerical Study of Oblique Shock-Wave/Boundary-Layer Interaction Considering Sidewall Effects," *Journal of Fluid Mechanics*, Vol. 767, 2015, pp. 526-561.
[32] Schülein, E., "Skin-Friction and Heat Flux Measurements in Shock/Boundary-Layer Interaction Flows," *AIAA Journal*, Vol. 44, No. 8, 2006, pp. 1732-1741.
[33] Moin, P., Squires, W., Cabot, W., and Lee, S., "A Dynamic Subgrid-Scale Model for Compressible Turbulence and Scalar Transport," *Physics of Fluids A*, Vol. 3, No. 11, 1991, pp. 2746 –2757.
[34] Ghosal, S., Lund, T. S., Moin, P., and Akselvoll, K., "A Dynamic Localization Model for Large Eddy Simulation of Turbulent Flows," *Journal of Fluid Mechanics*, Vol. 286, 1995, pp. 229-255.
[35] Fang, J., Li, Z., and Lu, L., "An Optimized Low-Dissipation Monotonicity-Preserving Scheme for Numerical Simulations of High-Speed Turbulent Flows," *Journal of Scientific Computing*, Vol. 56, 2013. pp. 67–95.
[36] Fang, J., Yao, Y., Li, Z., and Lu, L., "Investigation of Low-Dissipation Monotonicity-Preserving Scheme for Direct Numerical Simulation of Compressible Turbulent Flows," *Computers & Fluids*, Vol. 104, 2014, pp. 55–72.
[37] Fang, J., Yao, Y., Zheltovodov, A. A., Li, Z., and Lu, L., "Direct Numerical Simulation Of Supersonic Turbulent Flows Around A Tandem Expansion-Compression Corner, " Physics of Fluids, Vol. 27, No. 12, 2015.
[38] Lele, S. K., "Compact Finite Difference Schemes with Spectral-like Resolution," *Journal of Computational Physics*, 1992, Vol. 103, pp. 16-43.
[39] Gottlieb, S., and Shu, C. W., "Total Variation Diminishing Runge-Kutta Schemes," *Mathematics of Computation*, 1998, Vol. 67, pp. 73-85.
[40] Hung, C. M. and MacCormack., R. W. "Numerical Solution of Three-Dimensional Shock Wave and Turbulent Boundary-Layer Interaction," *AIAA Journal*, Vol. 16, 1978, pp. 1090–1096.
[41] Panaras, A. G., "Numerical Investigation of the High Speed Conical Flow Past a Sharp Fin," *Journal of Fluid Mechanics*, Vol. 236, 1992, pp. 607–633.
[42] Salin, A., Yao, Y., and Zheltovodov, A., "Flow Topology and Secondary Separation Modelling at Crossing Shock Wave/Turbulent Boundary-Layer Interaction Conditions," *International Journal of Aerospace Innovations*, Vol. 4, No. 1-2, 2012, pp. 13-27.
[43] Sagaut, P., "Theoretical Background: Large–Eddy Simulation," Large–Eddy Simulation for Acoustics, Cambridge University Press, Cambridge, 2007, pp. 89–127.
[44] Thomas, P. D., and Middlecoff, J. F., "Direct Control of the Grid Point Distribution in Meshes Generated by Elliptic Equations," *AIAA Journal*, Vol.18, No. 6, 1980, pp. 652-656.
[45] Kim, J. W., and Lee, D. J., "Generalized Characteristic Boundary Conditions for Computational Aeroacoustics." *AIAA Journal*, Vol. 38, No.11, 2000, pp. 2040-2049.
[46] Kim, J. W., and Lee, D. J., "Generalized Characteristic Boundary Conditions for Computational Aeroacoustics, Part 2." *AIAA Journal*, Vol. 1, No.1, 2004, pp. 47-55.

[47] Gloerfelt, X., and Lafon, P., "Direct Computation of the Noise Induced by a Turbulent Flow through a Diaphragm in a Duct at Low Mach number," *Computer & Fluids*, Vol. 37, 2008, pp. 388–401.
[48] Fang, J., Yao, Y., and Lu, L., "Preliminary Investigation of Three Dimensional Hypersonic Boundary Layer Flows," *UK Turbulence Consortium Annual Review 2013*, 2013, Southampton, UK.
[49] Lund, T. S., Wu, X. and Squires, K. D., "Generation of Turbulent Inflow Data for Spatially-Developing Boundary Layer Simulations," *Journal of Computational Physics*, Vol. 140, 1998, pp. 233-258.
[50] Sagaut, P., Garnier, E., and Tromeur, E., and Labourasse, E., "Turbulent Inflow Conditions for Large-Eddy Simulation of Compressible wall-Bounded Flows," *AIAA Journal*, 2004, Vol. 32, No. 3, pp. 469-477.
[51] Klein, M., Sadiki, A., and Janicka, J., "A Digital Filter Based Generation of Inflow Data for Spatially Developing Direct Numerical or Large Eddy Simulations," *Journal of Computational Physics*, Vol. 186, 2003, pp. 652–665.
[52] Morgan, B., Larsson, J., Kawai, S., and Lele, S. K., " Improving Low-Frequency Characteristics of Recycling/Rescaling Inflow Turbulence Generation," *AIAA Journal*, Vol. 49, No. 3, 2011, pp. 582–597.
[53] Wasistho, B., Geurts, B. J., Kuerten, J. G. M., "Simulation Techniques for Spatially Evolving Instabilities in Compressible Flow over a Flat Plate," *Computer & Fluids*, Vol. 26, 1997, pp. 713–739.
[54] Gao, F., Ma, W., Zambonini, G. Boudet, J., Ottavy, X., Lu, L., and Shao, L., "Large-Eddy Simulation of 3-D Corner Separation in a Linear Compressor Cascade," *Physics of Fluids*, Vol. 27, No. 8, 2015.
[55] Hornung. H.G., "Experimental Hypervelocity Flow Simulation, Needs, Achievements and Limitations," In: *First Pacific International Conference on Aerospace Science and Technology*, 1993, Taiwan.
[56] Spalart, P. R., "Direct Numerical Simulation of a Turbulent Boundary Layer Up to Re_θ=1410," *Journal of Fluid Mechanics*, Vol. 187, 1988, pp. 61-98.
[57] Wu, X., and Moin, P., "Direct Numerical Simulation of Turbulence in a Nominally Zero-Pressure-Gradient Flat-Plate Boundary Layer," *Journal of Fluid Mechanics*, Vol. 630, 2009, pp. 5-41.
[58] Pirozzoli, S., Bernardini, M., and Grasso, F., "Direct Numerical Simulation of Transonic Shock/Boundary Layer Interaction Under Conditions of Incipient Separation," *Journal of Fluid Mechanics*, Vol. 657, 2010, pp. 361-393.
[59] Purtell, L. P., Klebanoff, P. S., and Buckley, F. T., "Turbulent Boundary Layer at Low Reynolds Number," *Physics of Fluids*, Vol. 24, 1981, pp. 802-811.
[60] Erm, L. P., and Joubert, P. N., "Low Reynolds Number Turbulent Boundary Layers," *Journal of Fluid Mechanics*, Vol. 230, 1991, pp. 1-44.
[61] Salin, A., Yao, Y. F., and Zheltovodov, A. A., "Numerical Prediction of 3-D Supersonic Turbulent Separation Initiated by a Single-Fin," *29th International Symposium on Shock Waves*, Vol. 2, 2015, pp. 1265-1270.
[62] Pasha, A. A. and Sinha, K., "Simulation of Three-Dimensional Shock/Boundary-Layer Interaction in a Single-Fin Configuration," *11th Annual CFD Symposium. Bangalore*, 2009.
[63] Knight, D.D., Badekas, D., Horstman, C.C., and Settles, G.S., "Quasi-Conical Flow-field Structure of the Three-Dimensional Single Fin Interaction," *AIAA Journal*, Vol. 30, No. 12, 1992, pp. 2809-2816.
[64] Wu, M., and Martín, M.P., "Direct Numerical Simulation of Supersonic Turbulent Boundary Layer Over a Compression Ramp," *AIAA Journal*, 2007, Vol. 45(4): 879-889.
[65] Alvi, F.S., and Settles, G.S., "A Physical Model of The Swept Shock/Boundary-Layer Interaction Flowfield," *AIAA Journal*, Vol. 30, No. 9, 1992, pp. 2252–2258.
[66] Larsson, J., and Lele, S.K., "Direct numerical simulation of canonical shock/turbulence interaction," *Physics of Flids*, 2009, Vol. 21, No. 126101.
[67] Hsu, J., and Settles, G., "Holographic Flowfield Density Measurements in Swept Shock Wave/Boundary-Layer Interactions," *30th Aerospace Sciences Meeting and Exhibit*, 1992, AIAA Paper 92-0746.
[68] Fang, J., Lu, L.P., and Li, Z.R., "Direct Numerical Simulation of Shock-Turbulent Boundary Layer Interaction," *Physics of Gases*, 2013, Vol. 3, No. 8, pp. 23-36.
[69] Ringuette, M.J., Wu, M. and Martin, M.P., "Coherent Structures in Direct Numerical Simulation of Turbulent Boundary Layers at Mach 3," *Journal Fluid Mechanics*, 2008, 594:59-69.
[70] Moser, R.D., and Rogers, M.M. "Coherent Structures in A Simulated Turbulent Mixing Layer," Eddy Structure Identification in Free Turbulent Shear Flows, 1992, Poitiers, France: 415-428.
[71] Zhou, J., Adrian, R. J., Balachandar, S., and Kendall, T. M., "Mechanisms for Generating Coherent Packets of Hairpin Vortices in Channel Flow," *Journal of Fluid Mechanics*, Vol. 387, 1999, pp. 353-396.